A laser-triggered spark gap model

M. J. Kushner, R. D. Milroy, and W. D. Kimura
Spectra Technology, Inc. (Formerly Mathematical Sciences Northwest, Inc.), 2755 Northup Way, Bellevue, Washington 98004

(Received 18 March 1985; accepted for publication 7 June 1985)

Laser preionization is a method whereby the formative lag time and jitter of spark gaps can be reduced, and breakdown can be initiated at voltages significantly below the self-breakdown value. In the spark gaps of interest (100-ns spark duration), the plasma column expands from an initial laser preionized diameter of approximately 50 μm to an arc of diameter in excess of 1 mm, and conducts greater than 12-kA peak current. Since the time required for the resistive collapse of the plasma is comparable to the spark duration, the spark gap represents a non-negligible resistive loss in the circuit. The objective of this study is to understand the basic mechanisms by which laser-triggered spark gaps develop and to provide a basis to optimize their design and minimize their resistive losses. To study the expansion and conduction phases of laser-triggered spark gaps, a first principles model has been developed. This model includes gas dynamics, electron collision kinetics, radiation transport, and external circuitry in a self-consistent formulation. The formulation of the model is discussed and results are compared to experimental data. We find that growth of the spark column is dominated by gas dynamic expansion of the hot ionized core, augmented by photoionization and thermal ionization at the plasma column boundary. The plasma column is confined within a high-density cylindrical shell of neutral gas that traps ionizing radiation in a region of low E/N (electric field divided by gas density), thereby inhibiting expansion by nonhydrodynamic means (electron avalanche).

I. INTRODUCTION

Spark gaps are traditionally triggered by overvoltage or by internal auxiliary electrodes. The use of lasers as trigger sources for spark gaps has significant advantages over these methods.[1–9] Laser triggering of spark gaps has been demonstrated as a method whereby the formative lag time and jitter can be minimized, and whereby breakdown can be initiated at voltages significantly below the self–break value. In these devices, a laser with sufficient intensity to ionize the gas is focused between the electrodes of the device in order to initiate the electron avalanche and breakdown of the gas, (see Fig. 1). Although the potential across the spark gap may be insufficient to cause self-breakdown, once a plasma column is initiated by the laser, the voltage is sufficient to sustain and expand the column. The duration, location, and intensity of the laser can be carefully controlled, and therefore so can the time of breakdown of the spark gap.

In the laser-triggered spark gaps studied here the narrow-laser preionized column between the electrodes, initially of diameter $\approx 50\,\mu$m, expands to an arc with a diameter of 0.5–1.0 mm in approximately 100 ns, and carries a current in excess of 12 kA. During the spark expansion phase, the resistance of the plasma column decreases from many thousands of ohms to a few tenths of an ohm. For the applications of interest the load is a few ohms and the duration of the current pulse through the spark gap is about 100 ns, which is commensurate with the time required for column expansion. Therefore, during the electric current pulse, the plasma column changes from being a dominant resistive loss to being a relatively small resistive loss when compared to the load. The time required for this transformation to occur determines the amount of energy expended in the switch relative to that being delivered to the load. In order to optimize the performance, and minimize the losses, of laser-triggered spark gaps operating under these conditions, it is desirable to have a detailed understanding of the physics of the expansion phase of the spark.

Although many systematic studies of laser-triggered spark gaps have been performed[1–9] and some modeling has been done,[4,10] a first principles model of a laser-triggered spark column has not been presented. A first principles model would treat all the basic phenomena and make a minimum of *a priori* assumptions as to the thermodynamic state of the gas. This paper summarizes the first phase of development of a model to achieve that goal which, from first principles, describes the growth of the arc in a laser-triggered spark gap for a gas mixture of a noble gas and a diatomic molecule (e.g., Ar/H_2). Heavy particle gas dynamics, electron kinetics, radiation transport, and an external circuit are included in the analysis. Skin depth effects for the penetration of the applied electric field into the plasma are also included. Results from the model show that the expansion of the spark column is primarily by convection of the hot ionized core. An ionized channel of low-mass density is confined within a neutral high-mass-density compression (or shock) wave. The convective expansion of the core is augmented by photo and thermal ionization of the neutral gas at the interior of the high-mass-density shell. This finding agrees well with Braginskii's early theory of spark channel formation[11] and the theory of leader channel development by Kekez and Savic.[12] A companion experimental study of laser-triggered spark gaps using time-resolved laser interferometry also confirms these findings.[13]

Mechanisms by which the arc expands in a laser-triggered spark gap are discussed in Sec. II. The model is described in detail in Sec. III where issues pertaining to gas

 0021-8979/85/202988-13$02.40

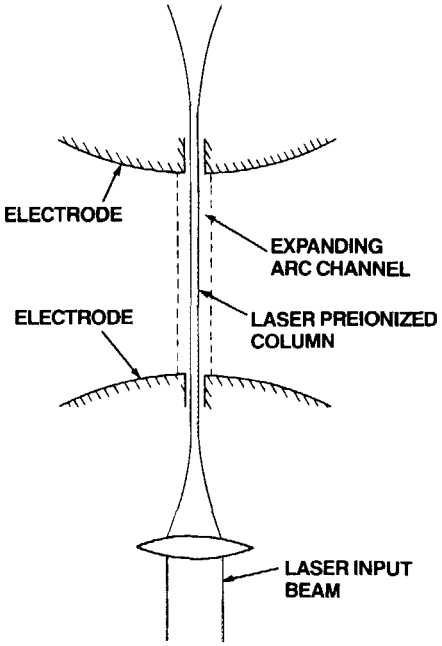

FIG. 1. Schematic of laser-triggered spark gap showing geometry used for the model.

dynamics, kinetics, and radiation transport are also discussed. The external circuit model is described in Sec. III as well. Simulated spark column characteristics are discussed in Sec. IV where comparisons are made to experimental data. Concluding remarks are in Sec. V. A listing and discussion of the continuity and conservation equations used in the model appear in the Appendix.

II. MECHANISMS FOR ARC EXPANSION IN LASER-TRIGGERED SPARK GAPS

The initial laser preionized column is approximately 50 μm in diameter and expands to an arc with a diameter in excess of 1 mm. The arc can expand by one or more of three mechanisms. In the first mechanism, a partially ionized fluid element convects from an inner radial point to an outer radial point. In doing so, the arc expands without requiring additional neutral gas to avalanche. In the next two mechanisms, electron avalanching is required for the arc to expand; electrons can diffuse from an inner radial point to an outer radial point, or local sources outside the plasma column can provide the seed electrons that initiate avalanching and subsequent rapid ionization of the gas. There are two local sources for seed electrons: photoionization and thermal ionization. Of the three arc column expansion mechanisms, the two dominant processes are convection and avalanching of neutral gas at the edge of the arc resulting from local sources of seed electrons. Convection increases the size of the arc without entraining additional mass into the plasma column, whereas electron avalanching of neutral gas at the edge of the plasma column does entrain additional mass.

As the gas temperature is raised in the core of the plasma column, the increase in thermodynamic pressure provides the driving force for a compression wave to propagate radially outwards and an expansion wave to propagate radially inwards. These gas dynamic waves accelerate the gas radially outward. At the outer boundary of the plasma column is a shock or compression wave that produces a thin region of gas with a mass density that is large as compared to the quiescent gas at larger radii. To a good approximation, the gas is compressed adiabatically by the shock wave and therefore has an associated increase in gas temperature. Typically the value of $\Delta\rho/\rho_0$ (change in mass density divided by the initial gas density) in the compression wave is larger than 3, and the gas temperature is increased to a value in excess of 1000 K. At these temperatures thermal ionization of the gas (as opposed to direct electron impact ionization of cold gas) becomes an important process. Although the rate of thermal ionization is many orders of magnitude less than that by electron impact ionization in the central core of the plasma column, it is important at the outer edge of the plasma column because there are no initially free electrons. In the absence of photoionization, thermal ionization is the only local source of seed electrons in this region. Once local free electrons are generated by thermal ionization, and in the presence of a sufficiently large applied electric field, the more rapid rate of electron impact ionization dominates that of thermal ionization and initiates a local electron avalanche. The nonconvective expansion of the plasma column then progresses radially outward as the current density of the newly avalanched region approaches that in the core of the plasma. The electron avalanche also serves to rapidly heat the heavy particles, thereby raising the local thermodynamic pressure and strengthening the gas dynamic processes.

Concurrent with thermal ionization in the adiabatically compressed gas, thermal dissociation also occurs. Locally, thermal dissociation is not important in directly providing an impetus for the electron avalanche to occur. The importance of thermal dissociation is manifested indirectly by changes in electron transport properties that may occur as a result of the relative change in atomic and molecular densities. For example, electron impact excitation of vibrational modes of the molecular species is one of the dominant nonionizing processes by which electrons lose energy and, hence, by which the electron temperature is constrained to a relatively low value. In the adiabatically heated region when a large fraction of the molecular species is thermally dissociated, the rate at which electrons lose energy as a result of vibrational excitation is smaller. This reduction allows a higher average electron temperature, a larger rate of electron impact ionization, and therefore a more rapid avalanching of the gas.

Photoionization, in analogy to thermal ionization, is not, on an absolute scale, an important source of ionization. The importance of photoionization is that it provides a local source of ionization in the neutral gas exterior to the highly ionized core of the plasma column. The radiation which produces photoionized seed electrons in the region exterior to the arc originates in the plasma within the arc. The transport of radiation from its source to the edge of the expanding plasma column where it is absorbed is therefore an important consideration. Radiation transport is included in our

model by separately treating optically thin and optically thick radiation. The formulation is discussed in Sec. III C.

III. DESCRIPTION OF THE MODEL, AND DISCUSSION OF GAS DYNAMIC, KINETIC, AND RADIATION TRANSPORT ISSUES

A. Gas dynamic and thermodynamic processes

The plasma is modeled as a single fluid having two temperatures: an electron temperature and a gas temperature. Conceptually, each temperature is associated with a specific fraction of the mass. When not collisionally dominated, one requires two fluids for an accurate description of the expansion process. For our collisionally dominated and ambipolar limited conditions, though, heavy particles (gas atoms and ions) and light particles (electrons) are sufficiently well coupled that a single fluid convective velocity suffices. This fact results from the high ion density, low rate of diffusion, and high heavy- particle-collision frequency.

The ion density in our spark columns is sufficiently high that electron transport is accurately described by the ambipolar approximation.[14] Using this approximation the diffusive motion of electrons is constrained to that of the ions, and the density of electrons and ions are locally equal. The low speed of diffusion of ions as compared to the convective velocity insures that the ions convect at the same velocity as other heavy particles. The high collision frequency between heavy particles insures that all heavy particles can be described with a single temperature.

With a single fluid, albeit with multiple temperatures, there is no relative motion between species. The convective velocity, although, is sufficiently large that the radial dimension of the region of interest may change by more than an order of magnitude during the electric current pulse while the entrained mass changes by a significantly smaller value. Under these conditions, a Lagrangian formulation of the transport equations is appropriate. Using this formulation, the fluid mass within each computational cell remains constant while the cell boundaries move with the convective velocity. In this manner, the density of mesh points tends to increase in regions of compression where gradients are likely to be large.

The fluid continuity, momentum, electron energy, and heavy-particle energy conservation equations used in the model are listed and discussed in the Appendix.

B. Kinetic processes

The gas dynamic and thermodynamic processes described in the previous section, and the equations in the Appendix, yield the fluid density, heavy-particle temperature, and electron temperature. The densities of individual species within the fluid are obtained from solution of the kinetic equations. The model treats a spark column in a mixture of a noble gas and a diatomic molecule. For the results discussed in this paper, the mixtures are Xe/H_2 and Ar/H_2. The species included in the model, functions of radial position and time, are listed in Table I. For atomic neutral and ionic species, the notation (n) in Table I indicates an excited state. For hydrogen, as many as ten states of the atom were used. Due to the large number of actual excited states for the noble gas,

TABLE I. Species included in the model.

Hydrogen:	H_2	$H_2(v)$, $v = 1,2$
	H_2^+	H_2^*, $\epsilon = 8.85$ eV, 12 eV
	H(n), $n = 1,10$	
Argon[a]:	Ar(n) I, $n = 1,11$	Ar(n) II, $n = 1,7$
	Ar(n) III, $n = 1,6$	Ar(n) IV, $n = 1,5$
	Ar(n) V, $n = 1,3$	Ar VI
	Ar_2^*	Ar_2^+

[a]Typical for noble gases.

states were grouped into pseudostates, comprising the actual states lying within an energy interval approximately 1500–3000 cm^{-1} wide. The statistical weights of the pseudostates are the sum of the statistical weights of the actual levels falling within the energy interval. The pseudo states used for the noble gas are listed in Ref. 15. Although the capability exists to include the noble gas for up to five times ionized, most of the results discussed here are for calculations where the highest ionization state included is doubly ionized, as the density of this state is sufficiently small that higher ionization states need not be included.

For computation of the electron temperature, collisional processes leading to excitation of two vibrational and two electronic states of H_2 were included, however, only the $v = 1$ vibrational state and H_2^* ($\epsilon = 8.85$ eV) electronic state were carried as kinetic variables. For our collisionally dominated plasmas, the lifetimes of higher states are very short. Including the electron impact process for excitation of the state while not including the state as a kinetic variable is equivalent to having an instantaneous relaxation of the state.

The processes included in the kinetics portion of the model are summarized in Table II. Conservation equations for each species were written using these processes with an additional correction term for changes in density by convection obtained from the continuity equation. In the Lagrangian formulation, the continuity equation provides the mass density in each computational cell, while maintaining a constant total mass in the cell. A fractional change in mass density in the cell, resulting from expansion or contraction of the cell boundaries, manifests a similar fractional change in the particle density of each species within the cell. The correction term mentioned above is the fractional rate of change in mass density times the number species density. A typical conservation equation for a kinetic species (i.e., an excited state of atomic hydrogen) used in the model is listed and discussed in the Appendix.

The electron frequency enters into the model in the three terms: electrical conductivity, electron thermal conductivity, and momentum transfer to heavy particles (i.e., gas heating). In a partially ionized plasma, the electron collision frequency ν_c is the weighted sum of the collision frequency with neutral particles ν_{cN} and with ions ν_{cI}.[16] The former frequency ν_{cN} is the product of the neutral particle density with the convolution of the momentum transfer cross section and the electron distribution function, in this case a Maxwellian with temperature T_e. The electrical conductivity of the partially ionized plasma is then

TABLE II. Electron impact and heavy particle collision rates.

Process	Rate[a]	Reference
$e + H_2 \rightarrow H_2 + e$	b	21
$e + H_2 \rightarrow H_2(v = 1,2) + e$	b	22[c]
$e + H_2 \rightarrow H_2^{*,**} + e$	b	23[c]
$e + H_2 \rightarrow 2H + e$	b	24
$e + H_2 \rightarrow H_2^+ + 2e$	$\epsilon = 15.4$ eV[d,e,h]	25,26
$e + H_2^* \rightarrow 2H + e$	$\epsilon = 12.0$ eV	f
$e + H_2^* \rightarrow H_2^+ + 2e$	$\epsilon = 3.4$ eV[d,e,h]	25,26
$e + H_2^+ \rightarrow H^+ + H + e$	b	27
$e + H(n) \rightarrow H(n) + e$	b	28
$e + H(n) \rightarrow H(n+1) + e$	$\epsilon_n = 13.6\,[1/n^2 - 1/(n+1)^2]$ eV[h]	25,26[c]
$e + H(n) \rightarrow H^+ + 2e$	$\epsilon = 13.6/n^2$ eV[d,e]	25,26
$e + H_2^+ \rightarrow 2H$	b	27
$e + Ar \rightarrow Ar + e$	b	29
$e + Ar(n) \rightarrow Ar(n+1) + e$	h	25,26[c]
$e + Ar(n)^Z \rightarrow Ar(1)^{Z+1} + 2e$	e,h	25,26
$e + Xe \rightarrow Xe + e$	b	29
$e + M^{Z+} \rightarrow M^{Z+} + e$	g	14
$e + M^{Z+} \rightarrow M^{(Z-1)+}$	$3.25(-13)T_e^{-0.7}$	32
$e + e + M^{Z+} \rightarrow M^{(Z-1)+} + e$	$3.6(-27)T_e^{-4.5}$ cm^6 s^{-1}	32
$e + Ar_2^+ \rightarrow Ar(n) + Ar(1)$	$6.56(-8)[1 - \exp(-3000/T_g)]T_e^{-2/3}$	33,34
$Ar + Ar^+ + M \rightarrow Ar_2^+ + M$	$3.0(-31)$ cm^6 s^{-1}	33
$H_2 + M \rightarrow H + H + M$	M = Ar $6.92(-6)T_g^{-1.025}\exp(-51992/T_g)$	31
	M = H_2 $2.95(-4)T_g^{-3/2}\exp(-51992/T_g)$	
	M = H $2.0(-6)T_g^{-1/2}\exp(-51992/T_g)$	
$M + [H_2^*, H_2(v=1)] \rightarrow M + 2H$	i	
$M + H_2^+ \rightarrow M + H^+ + H$	i	
$H_2(v=0) + M \rightarrow H_2(v=1) + M$	M = Ar $4.153(-28)T_g^{4.3}$	30
	M = H_2 $2.461(-27)T_g^{4.3}$	
	M = H $3.32(-10)\exp(-1369/T_g)$	
$M + M \rightarrow M^+ + M + e$	$1(-16)v_{th}\exp(-\epsilon_I/kT_g)$	j
$H^{**} + M \rightarrow H^* + M$	M = Ar,H $1(-18)$ cm^2	k
	M = H_2 $1(-17)$ cm^2	
$Ar^{**} + M \rightarrow Ar^* + M$	M = Ar,H $1(-18)$ cm^2	k
	M = H_2 $1(-17)$ cm^2	

[a] $5(-7) \equiv 5\times10^{-7}$. Rates are in units of cm^3 s^{-1} unless noted otherwise. T_e in eV, T_g in K.

[b] Cross section in indicated reference was averaged over a Maxwellian electron distribution function to obtain collision rate as a function of electron temperature.

[c] Reverse rates are by detailed balance.

[d] Rate is a function of threshold energy ϵ as indicated.

[e] Subject to lowering of ionization potential.

[f] Cross section and rate from Refs. 25 and 26 were used where the threshold energy is equal to the dissociation energy.

[g] See Sec. III B.

[h] Analytic form for the rate constant from Refs. 25 and 26 is a function of threshold energy ϵ(eV) and electron temperature T_e(eV). Typical ionization rate constant r for a single outer shell electron is

$$r = 2.35(-8)T_e^{1/2}\,u\psi(u), \quad u = \epsilon/T_e,$$

$$\psi(u) = \frac{\exp(-u)}{(1+u)}\left\{\frac{1}{(20+u)} + \ln\left[1.25\left(1+\frac{1}{u}\right)\right]\right\}.$$

The rate constant for electron excitation collisions for transitions with oscillator strength f is

$$r = 1.3(-6)\,T_e^{-3/2} f\psi(u)/u.$$

[i] Same rate as for H_2 except for Boltzmann factor with which the actual dissociation energy is used.

[j] ϵ_I is the ionization and v_{th} is the thermal velocity.

[k] Estimate.

$$\sigma = n_e e^2/[m_e(\nu_{cN} + \nu_{cI})], \tag{1}$$

where the electron density and mass are n_e and m_e, respectively. When the ion collision frequency is large compared to the neutral collision frequency, the conductivity approaches the Spitzer limit[16] σ_{SP} . For a singly ionized plasma,

$$\sigma_{SP} = 1.98e^2/m_e r_{eI}, \tag{2}$$

$$r_{eI} = \frac{\nu_{eI}}{n_e} = \frac{2.9\times 10^{-6}\ln(\Lambda)}{T_e^{3/2}},$$

$$\Lambda = 1.55\times 10^{10}\,(T_e^3/n_e)^{1/2}, \tag{3}$$

where the electron temperature has units of eV and the electron density has units of cm^{-3}. In this limit, the conductivity is a first-order function of electron temperature and has a weak dependence on electron density as a result of the appearance of n_e in the expression for Λ.

The derivation of Eqs. (2) and (3) assumes that there are many electrons within a Debye sphere.[16] Equivalently, this requirement is $\ln\Lambda \gg 1 \rightarrow n_e\lambda_D^3 \gg 1$, where λ_D is the Debye length. This condition requires that $\Gamma = n_e/T_e^{3/2} \ll 3$, where the electron density is in units of $10^{18}\ \mathrm{cm}^{-3}$ and the electron temperature is in eV. For our plasma conditions ($0.15 \leqslant \Gamma \leqslant 10$, $6 \geqslant \ln\Lambda \geqslant 2$), this inequality is not always satisfied. A first-order correction to Eq. (2) is to replace $\ln\Lambda$, which in itself is an approximation, with the exact expression

$$\ln\Lambda \rightarrow \int_0^{\Lambda} \frac{x^3}{(1+x^2)^2}\,dx = \frac{1}{2}\left(\ln(1+\Lambda^2) - \frac{\Lambda^2}{1+\Lambda^2}\right). \tag{4}$$

Further refinement in the value of conductivity requires a more detailed treatment.

For non-Debye plasmas ($\ln\Lambda \leqslant 1$), the conductivity is lower than the value one would calculate using the Spitzer value.[17,18] This results from electrons beginning to see the effect of the structure of the ion core. For small values of Λ, semiempirical and kinetic modeling yield an expression

$$\sigma = \sigma_{SP}\,(1 - 0.78/\Lambda^{2/3}) \tag{5}$$

which agrees well with experiment.[17]

C. Radiation processes and photoionization

The flux of radiation at location $\mathbf{r}$ of frequency ν, $\Phi(\mathbf{r},\nu)$, resulting from volumetric sources of radiation at location $\mathbf{r}'$, $S(\mathbf{r}',\nu)$, is given by

$$\Phi(\mathbf{r},\nu) = \int S(\mathbf{r}',\nu)\,\frac{\exp\left(-\int_{\mathbf{r}'}^{\mathbf{r}} \alpha_i(\mathbf{r}'',\nu)d\,|\mathbf{r}''-\mathbf{r}'|\right)}{4\pi|\mathbf{r}'-\mathbf{r}|^2}\,d^3r', \tag{6}$$

where $\alpha(\mathbf{r},\nu)$ is the photon absorption coefficient for frequency ν at location $\mathbf{r}$. The integral in Eq. (6) has, in general, no analytic solution if either the source function or absorption coefficient is a complex function of radius, a condition which prevails in our spark columns. The integral in Eq. (6) must therefore be performed numerically. The numerical procedures used in the model for the optically thin and optically thick limits of Eq. (6) (see below) are discussed in Ref. 15.

For the conditions of interest, photons generated within the plasma column can be classified as being either optically thick or optically thin. Optically thick photons are photons of sufficiently high energy that they are capable of ionizing ground-state species. Optically thin photons are photons of low enough energy that they cannot ionize ground-state species, but may be capable of ionizing excited states. These two photon groups naturally arise from the form of the photoionization states. For hydrogenic levels, the photoionization cross section scales as $(\epsilon_i^I/h\nu)^3$, where ϵ_i^I is the ionization potential of state i.[14] Photons with energy far in excess of threshold have a small photoionization cross section. For hydrogen and the noble gases, the ratio of the ionization potential of the ground state as compared to the first excited state is about 3–5. Therefore, photons which efficiently ionize the ground state do not have a large cross section for ionizing even the first excited state. Photons that are near threshold for ionizing excited states are not energetic enough to ionize ground states. For optically thin photons, the exponential function in Eq. (6) can be ignored. For optically thick photons, we can approximate that the absorption coefficient $\alpha(\mathbf{r},\nu)$ is constant over the short path between the point of emission and the point of observation.

For our conditions, the absorption coefficient is the sum of two dominant terms. The first, and of lesser importance in the partially ionized phase, is inverse bremsstrahlung or free–free absorption. When the plasma becomes fully ionized, and at longer wavelengths, inverse bremsstrahlung becomes the more important absorption mechanism. The absorption coefficient for this process in a plasma with temperature T is[14]

$$\alpha_{FF}(\nu) = \sum_i \left[\frac{4}{3}\left(\frac{2\pi}{3kT}\right)\frac{n_e N_i^+ Z_i^2 e^6}{hcm_e^{3/2}\nu^3} g_{FF}\right] \times\left[1 - \exp\left(\frac{-h\nu}{kT}\right)\right]\ \mathrm{cm}^{-1}, \tag{7}$$

where the factor $g_{FF} \approx 1$, N_i^+ is the density of ion i, and Z_i is the ionization state of ion i. The second and dominant absorption mechanism during the partially ionized phase is bound–free electron transitions, or photoionization. For hydrogenic states, the photoionization absorption coefficient for frequency ν with energy above threshold is approximately

$$\alpha_P(\nu) = \sum_i 7.9\times 10^{-18} N_i\,(\epsilon_i^I/h\nu)^3\ \mathrm{cm}^2. \tag{8}$$

In the model, photons were grouped into energy bins with widths of a few electron volts. When doing so, the absorption coefficient for a particular energy bin was the average value of Eqs. (7) and (8) over the energy range of interest.

Although line radiation is included as an energy loss mechanism (i.e., spontaneous emission), radiation transport is calculated only for the continuum component of the spectrum. The radiation source function $S(\mathbf{r},\nu)$ (photons/cm^3 s) for this continuum component results from free–bound radiative recombination and from bremsstrahlung. The former source is the more important source at lower electron temperatures and densities. The latter is the more important source at higher electron temperatures and densities. Assuming hydrogenic levels, the source function for free–bound radiation resulting from recombination of electrons with temperature T_e recombining into a level with ioniza-

tion potential ϵ^I and emitting radiation with energy between ϵ_k and ϵ_{k+1} is[14]

$$S_k = \sum_{\epsilon_k > \epsilon_j^I} n_e N^+ A(T_e) \int_{(2/m_e)(\epsilon_k - \epsilon_j^I)}^{(2/m_e)(\epsilon_{k+1} - \epsilon_j^I)} \frac{\exp(-\beta x) dx}{\left(\frac{1}{\gamma^2} + x\right)}, \quad (9)$$

where the summation is over all atomic and molecular states in the plasma that satisfy the energy criteria $\epsilon_k > \epsilon_j^I$, $\gamma^2 = m_e/(2\epsilon_j^I)$, and $\beta = m_e/(2kT_e)$. N^+ is the density of atoms in the next higher ionization state than the level to which recombination is occurring and $A(T_e)$ is a normalization constant to insure that the sum of photon sources equals the rate of radiative recombination. The source function for free–free (bremsstrahlung) radiation resulting from electrons colliding with ions can be found in Ref. 19.

D. Circuit equations

A schematic of the external circuit model is in Fig. 2. The companion experiment with which comparison is made utilizes a 1.5-Ω, 100-ns water pulse forming line (PFL).[13] The geometry of the spark gap chamber has approximately 20-nH fixed external geometrical inductance (L_E). The plasma column of length l has resistance R_P and inductance L_P. The load resistance (1.5 Ω) is R_L. The fixed parallel resistance R_f($\simeq$1000 Ω) is that associated with diagnostic probes. The resistance of the plasma column is

$$R_P = \left(l \int_0^{d/2} 2\pi r \frac{j(r)^2}{\sigma(r)} dr\right) \Big/ I^2, \quad (10)$$

where d is the column diameter, $j(r)$ is the current density, and $\sigma(r)$ is the electrical conductivity for radius r, and I is the total current through the column. The plasma column inductance is

$$L_P = \frac{2e}{I^2} \int_0^{d/2} \frac{B^2(r)}{4} dr + \frac{\mu_0}{2\pi} \ln\left(\frac{D}{d}\right) + L_p', \quad (11)$$

where the magnetic field at location r is

$$B(r) = \frac{2}{rc} \int_0^r j(r') 2\pi r' \, dr'. \quad (12)$$

In Eq. (11), D is the diameter of the current return path and L_p' is a fixed geometrical inductance. The total current through the spark column is the integral of the current density $j(r)$ over the cross-sectional area of the plasma. Due to skin depth and gas dynamic considerations, $j(r)$ is obtained by solution of

$$\frac{dj(r)}{dt} = u \frac{\partial j}{\partial r} + \frac{c^2}{4\pi} \frac{1}{r} \frac{\partial}{\partial r} \left[r \frac{\partial}{\partial r} \left(\frac{j(r)}{\sigma(r)} \right) \right] - \frac{c}{4\pi} \frac{1}{r} \frac{\partial}{\partial r} \left(r \frac{\partial}{\partial r} [u(r) B(r)] \right). \quad (13)$$

The circuit equations used in the model approximate the continuous PFL as a discrete pulse-forming (PFN) composed of capacitors and inductors. The details of modeling a PFN to simulate a PFL as applied to discharge problems are discussed in detail in Ref. 20. The pertinent circuit equations are

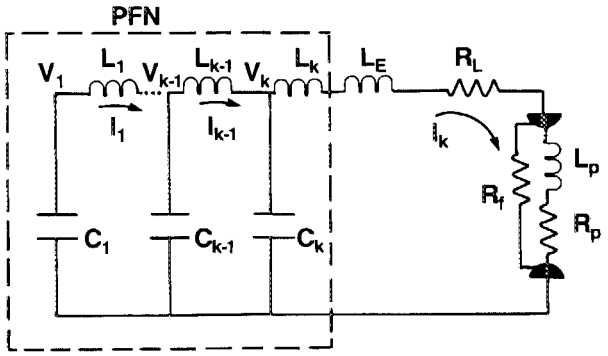

FIG. 2. Schematic of electrical circuit used in the model. The experimental pulse forming line is approximated by a pulse forming network (PFN). The spark column is represented by resistance R_P and inductance L_P.

$$\frac{dV_k}{dt} = -\frac{(I_k - I_{(k-1)})}{C_k}, \qquad \frac{dI_k}{dt} = \frac{[V_k - (V_P + IR_L)]}{(L_E + L_k)}, \quad (14)$$

where V_p is the voltage drop across the plasma. The subscripts k and $k-1$ denote values for the k th (the last) and $(k-1)$th stages at the termination of the PFN.[20] The voltage drop across the plasma column is

$$\frac{dV_P}{dt} = \frac{R_P R_f}{L_P} \left(I - \frac{V_P}{R_f} \right) + R_f \left(\frac{dI}{dt} \frac{V_P}{L_P} \right). \quad (15)$$

When L_P is small, $V_P = I(R_f R_P)/(R_f + R_P)$.

IV. SIMULATED SPARK COLUMN CHARACTERISTICS

In this section, simulated densities, temperatures, and circuit quantities for a spark column in a mixture of Xe/H_2:0.01/0.99 will first be examined. The initial gas pressure is 2 atm and the charging potential when laser triggered is 40 kV, close to the dc self-break voltage. The electrodes are separated by 1.2 cm and the current return path is 14 cm in diameter. The duration of the preionization pulse (<5 ns) is very short compared to the duration of the current pulse (>100 ns). Therefore, the initial electron density is assumed to appear instantaneously. The intent of this discussion is to illustrate general characteristics of laser triggered spark gaps. The issues discussed here apply to a wide range of initial conditions and gas mixtures; the details, of course, change.

A. Current and voltage, and spark column resistance

Experimental current and voltage traces,[13] and those computed with the model for similar conditions, are plotted in Fig. 3 for a laser-triggered spark column in a Xe/H_2:0.01/0.99 gas mixture having the properties listed above. The agreement between this model and experiment is generally good, however, the current is underpredicted. This discrepancy may result from overcorrecting for non-Debye effects or underpredicting the electron temperature. The voltage collapse time is approximately 25 ns, whereas the current rise time is in excess of 50 ns. The rate of current rise is

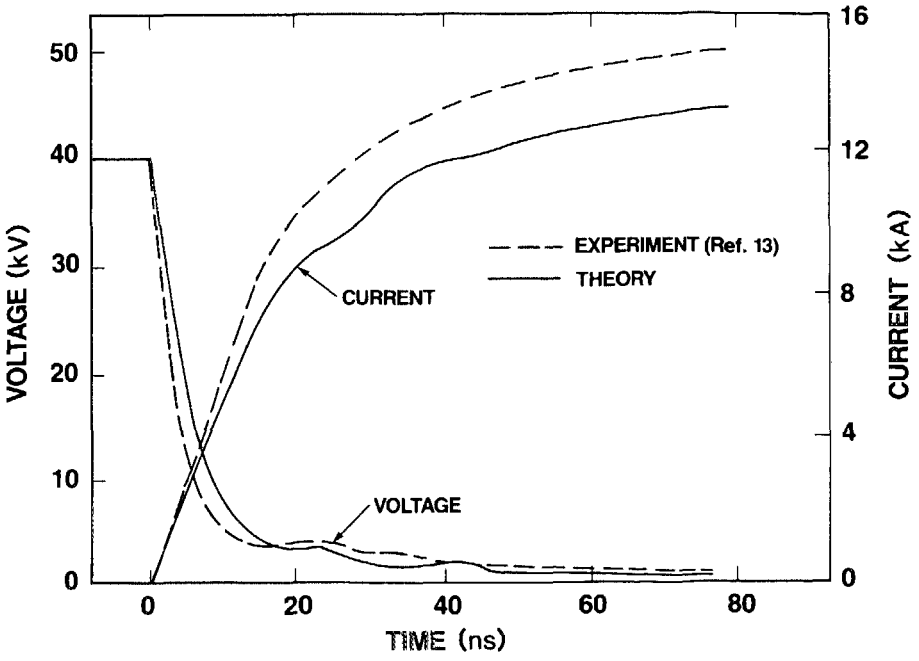

FIG. 3. Computed and experimental voltage and current for a laser-triggered spark column in a Xe/H_2:0.01/0.99 gas mixture. The initial pressure is 2 atm and the voltage at time of laser triggering is 40 kV. The electrode separation is 1.2 cm.

limited by the geometrical inductance of the spark gap chamber.

The resistance of the spark column is plotted in Fig. 4. The experimental curve for resistance was obtained by removing the inductive component of the measured voltage [i.e., $R = (V - L\,dI/dt)/I$]. Note that during the conduction phase of the spark gap, the voltage drop across the plasma column is in excess of 2 kV and the spark column resistance is a few tenths of an ohm. The rapid decrease in the resistance of the plasma column after breakdown results from avalanching and heating of the plasma. The slower decrease in resistance later in the pulse is a result of reaching the limit of Spitzer conductivity. The resistance then decreases as a result of a slower increase in the area of the plasma column caused by convective expansion.

The large voltage drop and resistance during the conduction phase of the current pulse as indicated in Figs. 3 and 4 have been verified experimentally.[35] In that experimental study, a coaxial capacitive voltage divider specifically designed for use with a spark gap having the geometry shown in Fig. 1 was used to measure the voltage drop across the spark column, and a current viewing resistor was used to measure the current. Interferograms of the expanding arc channel were used to determine the size of the arc and hence its inductance.[13] With these quantities, the time dependent resistance of arcs for a variety of gas mixes was obtained.

The average conductivity of the plasma column maximizes at about 40 ns ($\sigma \approx 5000\ \Omega^{-1}\ \mathrm{cm}^{-1}$) and subsequently begins to decrease. In the Spitzer limit, the conductivity is proportional to $T_e^{3/2}$. As the E/N across the plasma column decreases and the plasma expands, its temperature begins to decrease. This change in temperature reduces the average conductivity. The rate of expansion of the column (i.e., increasing its cross-sectional area) is sufficiently large to offset the decrease in conductivity. The result is a net slow decrease in the resistance of the plasma column.

B. Gas dynamic properties

The mass density of heavy particles for the arc discussed in Sec. IV A, is plotted in Fig. 5(a). The initial density is 2.7×10^{-4} g/cm^3. The same data is plotted in Fig. 5(b) in units of $\Delta\rho/\rho_0$. The pressure field for the same conditions is plotted in Fig. 6. The radial pressure gradient is the accelerating force for the convective velocity. The magnitude of the accelerating force is proportional to the density of contours in the radial direction of Fig. 6. The gas remains nearly motionless during the first 5 ns of the discharge pulse as this is the time required for the electron density to avalanche to a sufficiently large value to begin heating the heavy particles. Concurrent with the increase in gas temperature the gas

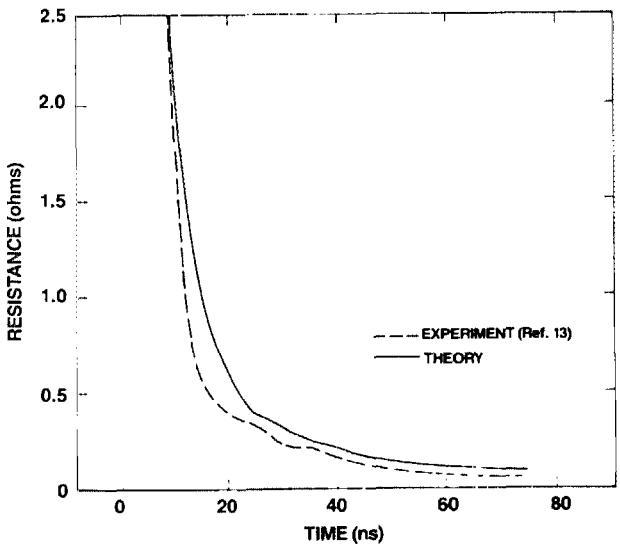

FIG. 4. Spark column resistance for the conditions of Fig. 3.

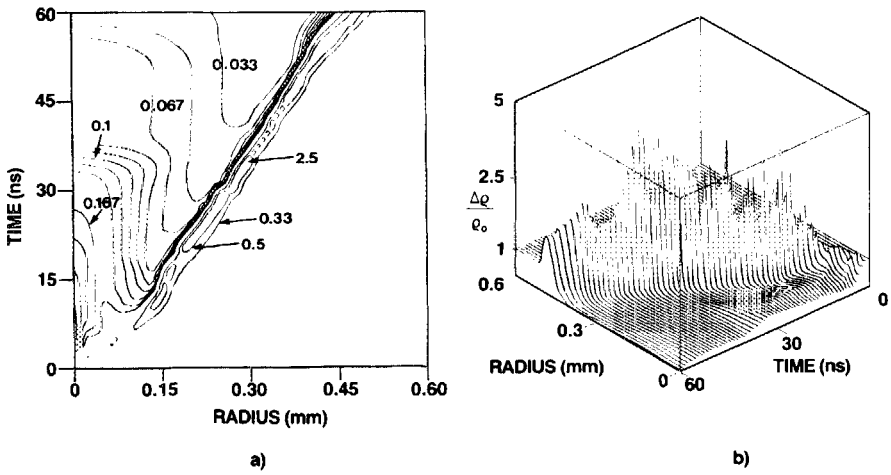

FIG. 5. Mass density for spark column having the conditions of Fig. 3. (a) Absolute mass density. The contour values are in units of 10^{-3} g cm^{-3} and the initial mass density is 2.7×10^{-4} g cm^{-3}. (b) Relative change in mass density in units of change in mass density divided by initial mass density.

pressure begins to increase, first near the axis and later at points with larger radii. The maximum pressure within the arc is approximately 1000 atm. This 500-fold increase in pressure comes from an increase in temperature by a factor of about 400 and four-fold increase in particle density (complete dissociation of H_2 and nearly complete ionization of H) coupled with a decrease in mass density by a factor of about three due to expansion.

The subsequently high-pressure gradient initiates convective motion of the gas radially outwards. As the hot gas moves outward, a low-density core is left behind and a region of increased heavy-particle density begins to form at the edge of the ionized region. Although colder than the ionized region, the pressure of this high-density gas increases to the point that it too begins to convect radially outward. At this point, a shock begins to form. The shock is initially strong ($\Delta\rho/\rho_0>5$) with a thin compressed gas layer (width <5 μm), and later weak ($\Delta\rho/\rho_0\leq5$) and with a thicker compressed gas layer (width $>30\,\mu$m). The mass density of the hot core is reduced to a value <0.05 that of its initial value, and the core is nearly isothermal with a temperature in excess of 50 000 K.

After the first 20 ns of convection, the pressure gradient within the core decreases leaving nearly isobaric conditions. As the arc continues to expand, pressure in the isobaric core slowly decreases. Steep pressure gradients are relegated to the outer regions of the arc. The transition between the core (pressures of many hundreds of atmospheres) and the cool gas exterior to the core (pressure of a few atmospheres) occurs across the shock-heated gas layer that has a thickness of only tens of microns. Radial profiles of the heavy-particle density as computed with the model and as measured interferometrically[13] are in Fig. 7. The agreement is quite good

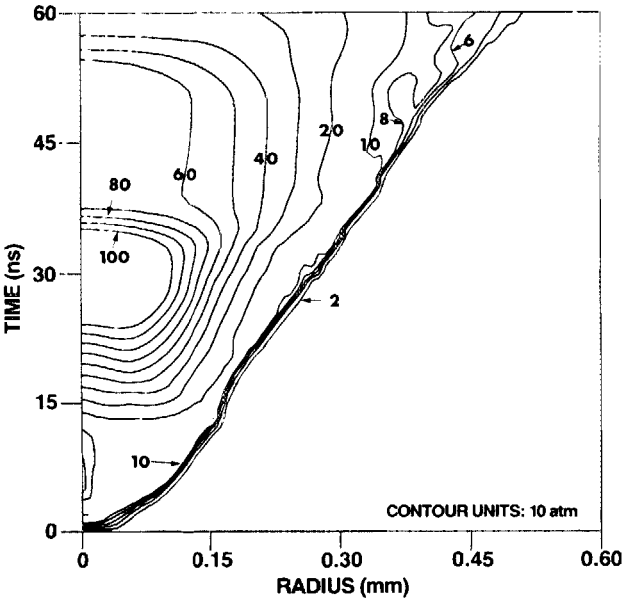

FIG. 6. Thermodynamic pressure for a spark column in a Xe/H_2:0.01/0.99 gas mixture.

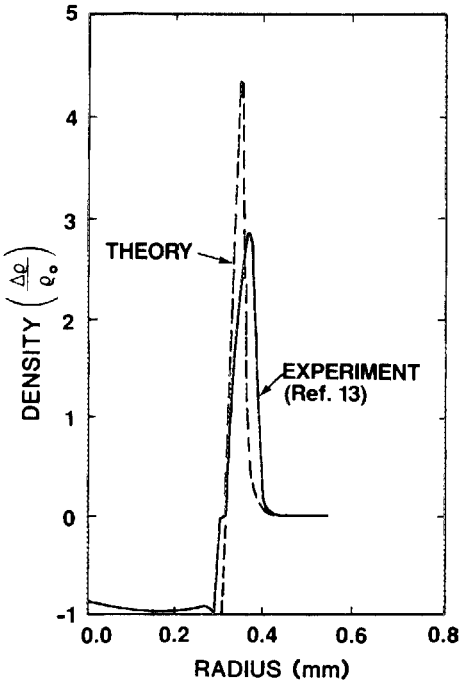

FIG. 7. Experimental and computed values for the relative change in mass density as a function of radius at $\simeq30$ ns after laser triggering. The depleted core and high-density shock wave are clearly shown.

and clearly shows the depleted core (in which the plasma column is confined) and the high density shell. The location of the maximum velocity is just interior to the shock front. At a particular radial location, the convective velocity monotonically increases in time to its maximum value. Although remaining positive, as the convective velocity decreases from its maximum value it may oscillate, responding to small changes in the pressure gradient. These pressure and velocity oscillations result in oscillations in the density rise across the shock front (see Fig. 5). The amplitude of the oscillation damps in time.

The shell of high neutral-particle density serves two nearly opposing functions: to both limit the rate of growth of the column and to provide the seed electrons required to avalanche the gas, thereby expanding the gas by nonconvective means. The accumulation of mass in the compressed gas layer increases the magnitude of the pressure gradient across the shock that is required to accelerate the accumulated mass. Therefore, the rate of expansion slows. The high-density shell is also a region with a low E/N which inhibits electrons in the shell from avalanching. In these respects, the high-density shell confines the arc. The high-density shell also serves as a source of seed electrons for avalanching which expands the arc by nonconvective means. The source of the seed electrons is trapping of ionizing radiation from the hot ionized core and thermal ionization resulting from adiabatic compression. The fact that the photoionization and thermal ionization occurs in a region of low E/N is unfortunate because the probability for avalanching is small with a low E/N.

The computed arc radius as a function of time appears in Fig. 8. (Arc radius obtained from the model is defined as the outer radius at which the current density falls to 0.1 that of the instantaneous maximum value.) Also plotted in Fig. 8 are results from the interferometric measurements,[13] and trajectories computed from the theories of Braginskii[11] and Dabora.[36] The agreement between this theory and experiment is good. The theories of Braginskii and Dabora overpredict the arc radius and show poor agreement. The poor agreement is possibly due to assumptions used by both Braginskii and Dabora which require a specific time dependence for power deposition and which are not strictly obeyed for our spark. Dabora's theory, though, does not take into account the fraction of the deposited energy that is expended ionizing, dissociating or otherwise exciting the gas, or energy that is radiated away. Other expressions for spark radius, based largely on Brakinskii's original formulation, have obtained good agreement with experiments; however, those treatments generally require experimental data to specify coefficients within the theoretical framework. Our model, though, requires no such coefficients. A review of theories which use semiempirical corrections to Brakinskii's expressions are in Ref. 37.

C. Electron, atomic, and molecular densities

The electron density for the spark column examined in the previous section is plotted in Fig. 9. The electron density reaches its maximum value near the axis and early during the discharge pulse before the heavy-particle density has been depleted by convection. As the gas convects radially outward, thereby lowering the mass density in the core, the electron density also decreases. The ionized fraction, though, increases during the duration of the spark. After 35 ns, the core is nearly fully ionized. For gas mixtures that are 99% hydrogen (as is the Xe/H_2:0.01/0.99 mixture discussed thus far), the electron temperature in the core exceeds 15 eV. For mixtures with a larger fraction of noble gas, the electron temperature is approximately 2–3 eV in. The high electron temperature results from the fact that after the molecular hydrogen has been dissociated and a significant fraction of the atomic hydrogen ionized, there is not a large density of species remaining with which electrons can have inelastic collisions. The remaining direct energy loss mechanisms are elastic collisions with ions ($2m_e/M_i$ energy loss) and radi-

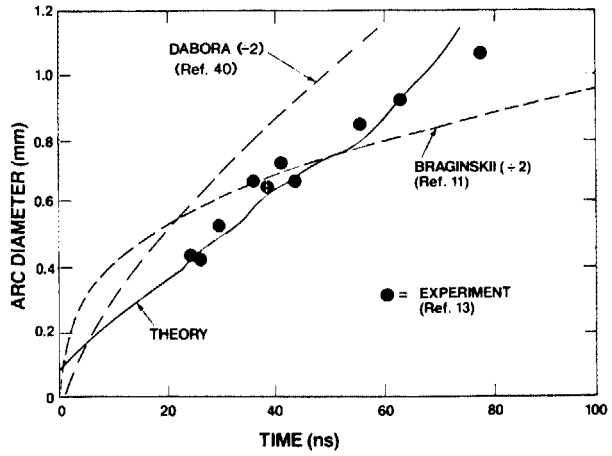

FIG. 8. Arc diameter as a function of time for a spark column with the conditions of Fig. 3. The experimental points were obtained from time resolved interferometric measurements. Note the change in scale for the theoretical results of Braginskii.

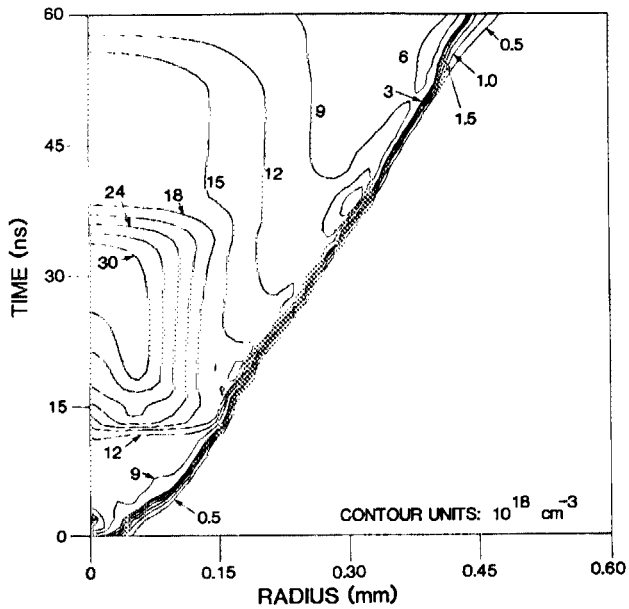

FIG. 9. Electron density for a spark column in a Xe/H_2:0.01/0.99 gas mixture.

ation. Cooling of the electrons occurs indirectly as thermal energy from the plasma is converted to kinetic energy of expansion of the column.

Although initially the most abundant neutral species, H_2 is a highly volatile species in the hot spark column environment. Dissociation proceeds by electron impact collisions and by thermal dissociation. The latter process requires only moderate heating of the gas (>5000 K) to result in significant dissociation. Once H_2 is dissociated a major electron energy loss mechanism, that of vibrational excitation, is eliminated, thereby enabling the electron temperature to climb to a higher value. The higher local electron temperature leads to rapid ionization.

This sequence of events is illustrated by Fig. 10. In the figure, the contours for H are for a density of 2×10^{18} cm^{-3} and for H_2 the contour line is for a density of 8×10^{18} cm^{-3}, and delineate the undisturbed gas, and the regions of dissociation and ionization. Also plotted is the region in which H_2^+ is found. At early times, before the gas has significantly heated or avalanched, molecular hydrogen is only depleted near the axis. Molecular hydrogen begins to first ionize and then dissociate. To the left of the low-density contour, H_2 is fully dissociated. The density of H_2 is high in the shock wave, however, the width of the region in which H_2 is at high density is narrower than that of the shock. (See Fig. 7.) This indicates that H_2 is thermally dissociating to atomic hydrogen at the inner side of the shock. After the first 25 ns, atomic hydrogen is primarily within and just interior to the shock. It is in this region where the gas is hot enough to fully dissociate H_2, however, the electron density is not yet high enough to deplete, by ionization, the atomic hydrogen. The density of H_2^+ proceeds through a similar, but even more volatile sequence. Early in the discharge, H_2^+ is the most abundant ion. As the gas heats and the electron density increases, H_2^+ is rapidly dissociated. The region in which the rate of ionization of H_2 exceeds the rate of dissociation and dissociative recombination of H_2^+ is confined to a very narrow portion of the shock.

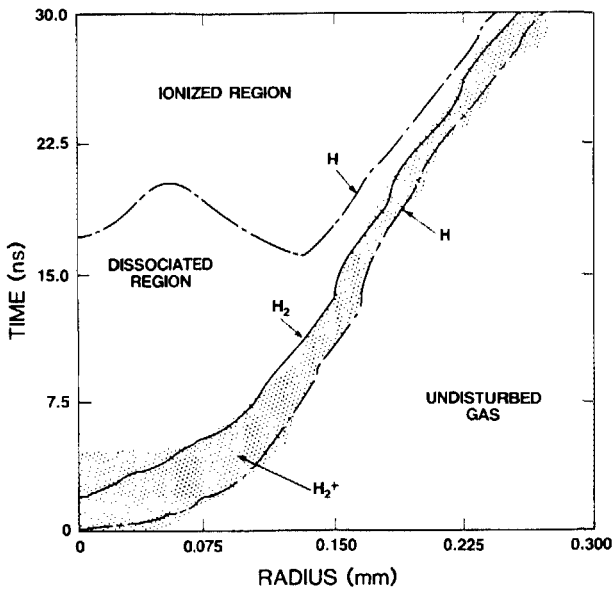

FIG. 10. Contours for atomic hydrogen (H), molecular hydrogen (H_2), and ionized molecular hydrogen (H_2^+) delineating region of the undisturbed gas, dissociated gas, and dominantly ionized gas.

D. The rate of arc expansion as a function of molecular weight

The sound speed of a gas at temperature T for an average molecular weight M is[38]

$$c_s = (\gamma kT/M)^{1/2}, \tag{16}$$

where γ is the ratio of specific heats. Since the dominant expansion mechanism for our spark columns is a gas dynamic sonic expansion of the hot plasma, the expansion rate can be affected by a change in plasma temperature or by a change in molecular weight of the gas. Arc radius as a function of time for three different Ar/H_2 gas mixtures is plotted in Fig. 11 to illustrate this affect. As the average molecular weight of the mixture increases, and the average sound speed decreases, the rate of arc expansion decreases. Note, though, that for the first 40 n after laser triggering, which includes a formative delay time, the rate of expansion for all cases is nearly identical. Although the heavy particles within the core are hot ($T_g > 15\,000$ K) there has been insufficient time for the pressure gradient to accelerate the particles to a significant velocity. During this period, radiation transport and subsequent photoionization of the neutral gas outside the plasma column are responsible for expansion of the arc. As the gas accelerates, convection becomes the dominant expansion mechanism. At this time, the expansion rate for plasmas with different molecular weights begins to diverge. The gas mixture with the lower average molecular weight, and corresponding higher sound speed, expands at the higher rate.

The rate of arc expansion can also be a function of both the magnitude and rate of energy deposited in the plasma. Computed mass density and arc radii for spark columns having different values of charging voltage at the time of laser triggering are plotted in Fig. 12. The rate of arc expansion increases with increasing charging voltage and increasing rate of energy deposition. The strength of the shock also

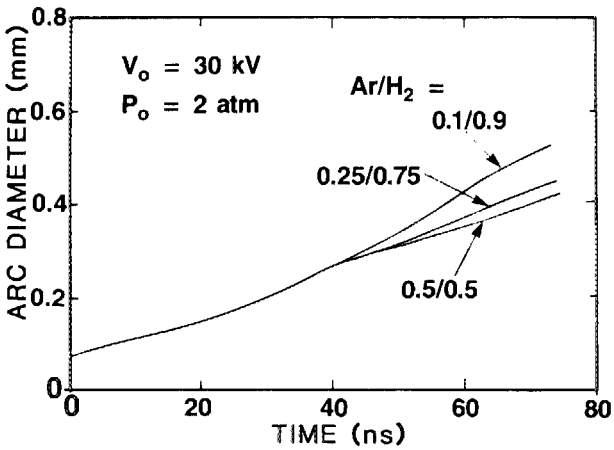

FIG. 11. Arc diameter for spark columns in mixtures of Ar/H_2 demonstrating the effect of molecular weight on the rate of expansion. To the extent that the arc grows by sonic expansion, the growth rate is inversely proportional to the average molecular weight of the gas mixture.

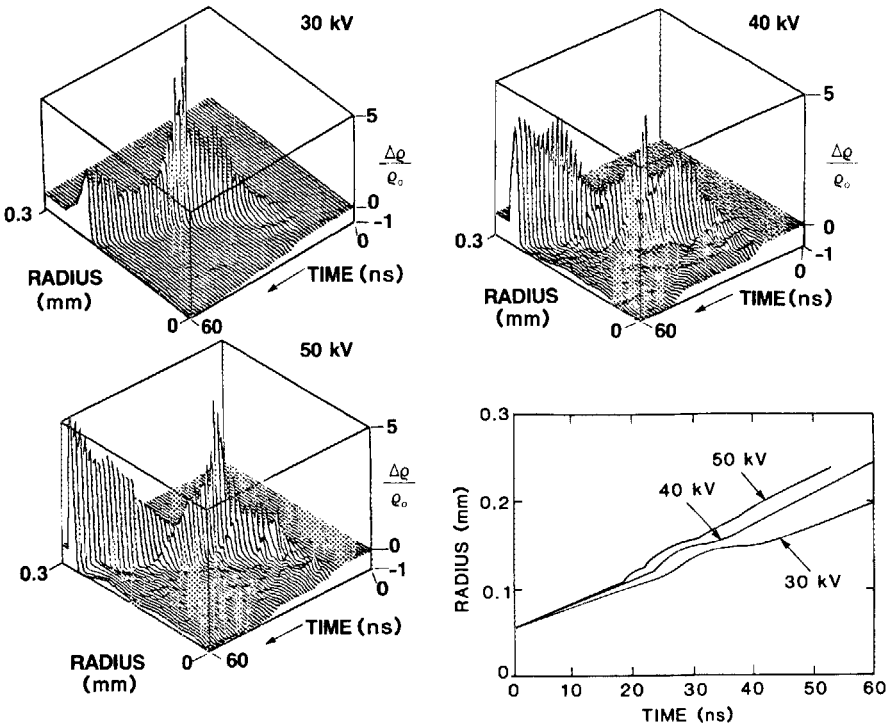

FIG. 12. Arc diameter and mass density for an Ar/H_2:0.25/0.75 gas mixture for different charging voltages at the time of laser triggering. For larger voltages, the rate of arc expansion is higher and the strength of the shock wave is greater.

increases with increasing charging voltage. The increasing strength of the shock is indicated by the decreasing thickness of the shock and the increase in compression ratio across shock with increasing voltage at laser triggering.

V. CONCLUDING REMARKS

A first principles model for arc expansion in a laser-triggered spark gap has been developed and comparison to experimental measurements shows good agreement. The growth of the arc from the laser preionized diameter of ≈ 50 μm to greater than 1 mm in less than 100 ns proceeds primarily as a convective expansion of the hot ionized plasma column. The rate of expansion is only marginally increased by photo and thermal ionization. This results from the high-density shell of neutral gas which confines the plasma column, and with its low E/N, inhibits arc expansion by electron avalanche. Electron temperatures in gas mixtures of 99% hydrogen exceed 15 eV, while more moderate electron temperatures of 2–3 eV are the norm for mixtures with a few percent or more of a heavy noble gas. The plasma voltage drop computed for sparks carrying in excess of 10 kA is rather large (a few kilovolts) and agrees well with experimental data.

ACKNOWLEDGMENTS

This work was supported by the Office of Naval Research (Contract No. N00014-83-0417) and the Naval Surface Weapons Center (Contract No. N60921-83-C-4057). The authors would like to thank Dr. S. R. Byron of Spectra Technology, Inc. (STI) for his critical review of the manuscript and Dr. J. J. Ewing of STI for his technical direction. Assistance from Jonathan Seamans and Dennis Ford during the supporting experiments is also gratefully acknowledged.

APPENDIX: CONTINUITY AND CONSERVATION EQUATIONS

The continuity and momentum conservation equations used in the model are

$$\frac{d\rho}{dt} = -\frac{\rho}{r}\frac{\partial}{\partial r}(ru), \tag{A1}$$

$$\frac{du}{dt} = -\frac{1}{\rho}\frac{\partial}{\partial r}\left[\left(\sum_i Z_i\rho/\sum_i \rho\right)\nabla P_e + \nabla P\right] - \frac{1}{\rho}\frac{B}{4\pi}\frac{1}{r}\frac{\partial}{\partial r}(rB), \tag{A2}$$

where u is the radial convective velocity, P_e is the electron gas pressure, P is the heavy-particle gas pressure, and B is the axial magnetic field. In Eq. (A2), the sum is over heavy species and Z_i is the charge state of species i. The first term in Eq. (A2) accounts for the fact that the force exerted by the pressure gradient ∇P_e acts only on the ionized mass fraction of the heavy particles through the radial ambipolar electric field. The last term in Eq. (A2) is due to the effect of self-generated electromagnetic fields and is the source of the compressive force in "pinch" plasmas. For our collisionally dominated conditions, this effect is not important.

Separate energy equations were written for the electrons and the heavy particles. The electron energy conservation equation is

$$\frac{d\left(\frac{3}{2}n_e kT_e\right)}{dt} = -P_e\frac{1}{r}\frac{\partial}{\partial r}(ru) + \frac{1}{r}\frac{\partial}{\partial r}\left(r\lambda_e\frac{\partial T_e}{\partial r}\right) + J^2/\sigma - \tfrac{3}{2}n_e k(T_e - T_g)\sum_i N_i(2m/M_i)\nu_{ci}$$

$$- \sum_{ij}\epsilon_{ij}n_e\left[N_i - N_j\exp(\epsilon_{ij}/kT_e)\right]r_{ij} - \sum_i n_e N_i\, r_i^I\left(\tfrac{3}{2}kT_e + \epsilon_i^I\right)$$

$$+ \sum_{ij} n_e^2 N_i^{+}\, r_{ij}^c\left(\tfrac{3}{2}kT_e + \epsilon_j^I\right) - \sum_{ij} n_e N_i^{z+}\, r_{ij}^r\left(\tfrac{3}{2}kT_e\right) - \sum_i \kappa n_e Z_i^2 N_i\, T_e^{1/2}$$

$$+ \sum_i \int N_i\Phi(\nu)\,\sigma_i^I(\nu)(h\nu - \epsilon_i^I - \tfrac{3}{2}kT_e)d\nu. \tag{A3}$$

In Eq. (A3), n_e is the electron density, T_e is the electron temperature, λ_e is the electron thermal conductivity, J is the current density, σ is the electrical conductivity, ϵ_{ij} is the energy separation between species i and j, and ϵ_i^I is the ionization potential of species i. The electron mass and mass of species i are m_e and M_i, respectively, and the gas temperature is T_g. The rate constant for excitation of heavy-particle species N_i to N_j is r_{ij}, the rate constant for ionization of N_i is r_i^I, the rate constant for collisional radiative recombination of ion N_i^{z+} to form species $N_i^{(z-1)+}$ is r_{ij}^c, and the analogous rate constant for radiatve recombination is r_{ij}^r. ν_{ci} is the electron collision frequency with species i, and $\sigma_i^I(\nu)$ is the photoionization cross section of species i for frequency ν by photon flux $\Phi(\nu)$.

The terms in Eq. (A3) (in order of presentation) are for heating of the electrons by adiabatic compression, thermal conduction, joule heating, thermalization of electrons with the heavy particles, inelastic and superelastic excitation collisions with heavy particles, ionization collisions with heavy particles, electron heating due to collisional radiative recombination, energy loss due to radiative recombination, energy loss due to bremsstrahlung radiation, and energy inputs to the electron distribution resulting from photoionization. In the term for bremsstrahlung loss the rate constant $\kappa = 10^{-13}\ \mathrm{eV}^{1/2}\ \mathrm{cm}^3\ \mathrm{s}^{-1}$ which yields an energy loss that is small compared to joule heating. The thermal conduction term serves to smooth the electron temperature distribution as a function of position. However, because electron transport is dominated by collisions with heavy particles, this term is not particularly important.

The heavy-particle energy conservation equation is

$$\frac{d(\rho c_p T_g)}{dt} = -P\frac{1}{r}\frac{\partial}{\partial r}(ru) + \frac{1}{r}\frac{\partial}{\partial r}\left(r\lambda_g\frac{\partial T_g}{\partial r}\right)$$

$$+ \tfrac{3}{2}n_e k(T_e - T_g)\sum_i N_i(2m/M_i)\nu_i - \sum_{i,j,k,l}\epsilon_{ijkl}\left[N_iN_j - N_kN_l\exp\left(\frac{\epsilon_{ijkl}}{kT_g}\right)\right]r_{ijkl}^H, \tag{A4}$$

where c_p is the heavy-particle specific heat and λ_g is the heavy-particle thermal conductivity. The terms of Eq. (A4) are for heating from adiabatic compression, heat transport due to thermal conduction, and joule heating by collisions with hot electrons. In the last term of Eq. (A4), for changes in internal energy due to heavy-particle collision processes, r_{ijkl}^H is the endothermic rate at which reactants i and j collide, resulting in product species k and l (e.g., $H_2 + M \rightarrow H + H + M - \epsilon$). The activation energy for the process is ϵ_{ijkl}.

A typical conservation equation for a kinetic species (i.e., an excited state of atomic hydrogen) as used in the model is

$$\frac{\partial H_i}{\partial t} = \sum_j n_e(r_{ji}H_j - r_{ij}H_i) - n_e\, r_i^I H_i + n_e\,(r_i^r + r_i^{cr}n_e)H^+$$

$$+ n_e\{r_d'\,H_2^+(\delta_{i1} + \delta_{in}) + 2r_d[H_2 + H_2(v)]\delta_{i1} + r_d\,\mathrm{H}_2^*(\delta_{i1} + \delta_{ni})\}$$

$$- \sum_k N_k\left[\sum_j (r_{ji}^h H_j - r_{ij}^h H_i)\right] + 2r_{dk}^{\mathrm{H}_2}H_2\delta_{i1} + 2r_{dk}^{\mathrm{H}_2(v)}H_2(v)\delta_{i1}$$

$$+ 2r_{dk}^{\mathrm{H}_2^*}(\delta_{i1} + \delta_{ni}) + r_{dk}^{\mathrm{H}_2^+}\delta_{i1} - \sum_l r_k^{ra}H_lH_i + \frac{H_i}{\rho}\frac{d\rho}{dt}. \tag{A5}$$

In Eq. (A5), δ_{ni} denotes that the process pertains only to the hydrogen-excited state $n = i$ and N_k denotes a third body which has associated with it a unique rate constant also having subscript k. The following terms of Eq. (A5), in order of presentation, have rate constants that are functions of electron temperature: electron excitation of H_i from level H_j (rate constant r_{ji}); electron collisional relaxation of H_i to H_j r_{ij}); electron impact ionization of $H_i(r_i^I)$; recombination of H^+ populating H_i by radiative recombination (r_i^r) and by collisional radiative recombination (r_i^{cr}); dissociative recombination of H_2^+ populating $H(1)$ and a higher excited state (r_d'); electron impact dissociation of H_2, $H_2(v)$, and H_2^* (r_d). The remaining terms of Eq. (A5), in order of presentation, have rate constants that are functions of heavy-particle temperature: collisional quenching by heavy particles of a higher lying level j to $H_i(r_{ji}^h)$ and of H_i to a lower level $j(r_{ij}^h)$; thermal dissociation of H_2, $H_2(v)$, H_2^*, and H_2^+ (rate constants $r_{dk}^{\mathrm{H}_2}$, $r_{dk}^{\mathrm{H}_2(v)}$, $r_{dk}^{\mathrm{H}_2^*}$, $r_{dk}^{\mathrm{H}_2^+}$); and reassociation of H atoms to form H_2. The last term in Eq. (A5) is the correction to the density of H_i resulting from convection. The rate of thermal ionization of species i was approximated by $r_{gk}\exp(-\epsilon_i^I/kt_g)$, where r_{gk} is the gas kinetic rate constant.

[1]L. P. Bradley and T. J. Davies, IEEE J. Quantum. Electron. **QE-7**, 464 (1967).
[2]K. Harsch, H. Salzmann, and H. Strohwald, Phys. Lett. A **55**, 153 (1975).
[3]A. G. Akmanov, L. A. Rivlin, and V. S. Shil'dyaev, JETP Lett. **8**, 258 (1968).
[4]A. H. Guenther and J. R. Bettis, J. Phys. D **11**, 1577 (1978).
[5]W. R. Rapoport, J. Goldhar, and J. R. Murray, IEEE Trans. Plasma Sci. **PS-8**, 167 (1980).
[6]J. R. Woodworth, R. G. Adams, and C. A. Frost, IEEE Trans. Plasma Sci. **PS-10**, 257 (1982).
[7]J. R. Woodworth, C. A. Frost, and T. A. Green, J. Appl. Phys. **53**, 4734 (1982).
[8]J. Goldhar, W. R. Rapoport, and J. R. Murray, IEEE J. Quantum Electron. **QE-16**, 235 (1980).
[9]R. A. Dougal and P. F. Williams, J. Phys. D **17**, 903 (1984).
[10]R. A. Dougal and P. F. Williams, J. Phys. D (to be published).
[11]S. I. Braginskii, Sov. Phys. *JETP* **34**, 1068 (1958).
[12]M. M. Kekez and P. Savic, "Contributions to Continuous Leader Channel Development," in *Electrical Breakdown and Discharges in Gases*, edited by E. E. Kunhardt and L. H. Luessen (Plenum, New York, 1983), pp. 419–454.
[13]W. D. Kimura, E. A. Crawford, M. J. Kushner, and S. R. Byron, "Investigation of Laser Preionization Triggered High Power Switches Using Interferometric Techniques," in *Conference Record of 1984 Sixteenth Power Modulator Symposium*, Arlington, VA (IEEE, New York, 1984), p. 54.
[14]M. Mitchner and C. H. Kruger, *Partially Ionized Gases* (Wiley-Interscience, New York, 1973).
[15]M. J. Kushner and R. D. Milroy, "Spark Column Plasma Dynamic Model—Final Report," Mathematical Sciences Northwest, Inc., Contract No. N00014-83-C-0417 (Sept. 1984).
[16]L. Spitzer, Jr., *Physics of Fully Ionized Plasmas* (Wiley-Interscience, New York, 1967).
[17]V. A. Alekseev, V. E. Fortov, and I. T. Yakubov, Sov. Phys. Usp. **26**, 99 (1983).
[18]R. E. Rovinskii, Teplofiz. Vysok. Temp. **10**, 1 (1972).
[19]C. L. Longmire, *Elementary Plasma Physics* (Wiley-Interscience, New York, 1967).
[20]M. J. Kushner, A. L. Pindroh, C. H. Fisher, T. A. Znotins, and J. J. Ewing, J. Appl. Phys. **58**, 2406 (1985).
[21]D. K. Gibson, Aust. J. Phys. **23**, 683 (1970).
[22]G. J. Schulz, Phys. Rev. **135**, A983 (1964).
[23]A. G. Engelhardt and A. V. Phelps, Phys. Rev. **131**, 2115 (1963).
[24]S. J. B. Corrigan, J. Chem. Phys. **43**, 4381 (1965).
[25]H. W. Drawin, European CEA Report No. FC-387, 1967; European CEA Report No. FC-383, 1966.
[26]C. Deutsch, J. Appl. Phys. **44**, 1142 (1973).
[27]C. F. Chan, "Reaction Cross Sections and Rate Coefficients Related to the Production of Positive Hydrogen Ions," Lawrence Berkeley Laboratory LBID-632 (1983).
[28]Y. Itikawa, Planet. Space Sci. **19**, 993 (1971).
[29]L. S. Frost and A. V. Phelps, Phys. Rev. **136**, A1538 (1964).
[30]N. Cohen and J. F. Bott, "Review of Rate Data for Reactions of Interest in HF and DF Lasers," Aerospace Corporation Rep. No. SD-TR-82-86 (Oct. 1982).
[31]V. N. Kondratiev, *Rate Constants of Gas Phase Reactions*, NTIS COM-72-10014 (National Bureau of Standards, Washington, DC, 1972).
[32]M. A. Biondi, "Recombination," in *Principles of Laser Plasmas*, edited by G. Bekefi (Wiley, New York, 1976), pp. 125–157.
[33]Ch. A. Brau, "Rare Gas Halogen Excimers," in *Excimer Lasers*, edited by Ch. K. Rhodes (Springer, Berlin, 1979), pp. 104–105.
[34]T. F. O'Malley, Phys. Rev. **185**, 101 (1969).
[35]M. J. Kushner, W. D. Kimura, and S. R. Byron, J. Appl. Phys. **58**, 1744 (1985).
[36]E. K. Dabora, AIAA J. **10**, 1384 (1972).
[37]J. D. Craggs, "Spark Channels," in *Electrical Breakdown of Gases*, edited by J. M. Meek and J. D. Craggs (Wiley, Chichester, UK, 1978), pp. 801–821.
[38]P. A. Thompson, *Compressible-Fluid Dynamics* (McGraw-Hill, New York, 1972).